

Characterization of *in vivo* MRI detectable thalamic amyloid plaques from APP/PS1 mice

Marc Dhenain^{a,b,c,*}, Nadine El Tannir El Tayara^{b,c}, Ting-Di Wu^{b,c}, Maryvonne Guégan^d,
Andreas Volk^{b,c}, Carmen Quintana^{b,c,e}, Benoît Delatour^d

^a URA CEA CNRS 2210, I2BM, SHFJ, 4 Place du Général Leclerc, 91401 Orsay Cedex, France

^b U759 INSERM, Centre Universitaire, Laboratoire 112, 91405 Orsay Cedex, France

^c Institut Curie, Centre Universitaire, Laboratoire 112, 91405 Orsay Cedex, France

^d Laboratoire NAMC, CNRS, UMR 8620, Bât 446, Université Paris Sud, 91405 Orsay, France

^e Instituto de Microelectronica de Madrid-CSIC, 8, Isaac Newton, 28760 Tres Cantos, Madrid, Spain

Received 11 September 2006; received in revised form 10 April 2007; accepted 17 May 2007

Available online 27 June 2007

Abstract

Amyloid deposits are one of the hallmarks of Alzheimer's disease. Recent studies, in transgenic mice modeling Alzheimer's disease showed that, using *in vivo*, contrast agent-free, MRI, thalamic amyloid plaques are more easily detected than other plaques of the brain. Our study evaluated the characteristics of these thalamic plaques in a large population of APP/PS1, PS1 and C57BL/6 mice. Thalamic spots were detected in all mice but with different frequency and magnitude. Hence, the prevalence and size of the lesions were higher in APP/PS1 mice. However, even in APP/PS1 mice, thalamic spots did not occur in all the old animals. In APP/PS1 mice, spots detection was related to high iron and calcium load within amyloid plaques and thus reflects the ability of such plaque to capture large amounts of minerals. Interestingly, calcium and iron was also detected in extra-thalamic plaques but with a lower intensity. Hypointense lesions in the thalamus were not associated with the iron load in the tissue surrounding the plaques, nor with micro-hemorrhages, inflammation, or a neurodegenerative context.

© 2007 Elsevier Inc. All rights reserved.

Keywords: Alzheimer's disease; Animal models; Amyloid; APP; Calcium; Iron; Mineralization; MRI; PS1; Transgenic mouse

1. Introduction

Senile plaques are one of the neuropathological hallmarks of Alzheimer's disease (AD). These microscopic lesions are extracellular deposits of amyloid- β (A β) peptides surrounded by glial cells and dystrophic neurites. Their detection by histology is based on the use of specific dyes or antibodies directed against A β epitopes. Their detection by *in vivo* MRI is a challenge that might help diagnosing and following the pathology.

Several studies at high magnetic field have shown that amyloid plaques from various brain regions (isocortex,

hippocampus, thalamus) can be detected as hypointense structures by MRI without contrast agent (Braakman et al., 2006; Jack et al., 2004; Lee et al., 2004; Vanhoutte et al., 2005). These studies also highlighted the particular behavior of a subset of thalamic plaques that are more easily detected by *in vivo* MRI than plaques from the isocortex or hippocampus. Indeed in these studies, thalamic plaques appeared to be larger than the isocortical/hippocampal plaques on the MR images (Jack et al., 2004) and can be detected by MRI even when the isocortical/hippocampal plaques are not visible (Vanhoutte et al., 2005). Two previous studies described more finely the nature of MRI-detected thalamic plaques and revealed their association with very dense iron aggregates (Jack et al., 2004; Vanhoutte et al., 2005). These two studies were however performed on a small number of animals and did not focus on the exact nature/origin of these neuropathological lesions neither on their association with

* Corresponding author at: URA CEA CNRS 2210, I2BM, SHFJ, 4 Place du Général Leclerc, 91401 Orsay Cedex, France. Tel.: +33 1 69 86 77 58; fax: +33 1 69 86 77 45.

E-mail address: Marc.Dhenain@cea.fr (M. Dhenain).

overall levels of brain amyloidosis. In the present study, we tried to characterize these thalamic alterations, using different complementary approaches (MRI, neurohistology, ultrastructural and elemental analyses) in a large population of APP/PS1 and control PS1 or C57BL/6 mice, at various ages corresponding to graded neuropathological stages. We showed that thalamic spots occur only in a subpopulation of APP/PS1 mice and that they are related to a ferro-calcification of the amyloid deposits leading to the presence of dense aggregates in their core.

The mechanisms associated with the modifications of the thalamic plaques detected by MRI were assessed in a second part of the study. First, because amyloid deposits can trap endogenous iron (El Tannir El Tayara et al., 2006), it is possible that local increased iron loads in plaque-enriched areas (i.e. thalamus) is a causative factor. To address this possibility we assessed correlations between iron levels in the thalamus and the occurrence of hypointense spots and ferrocyclic aggregates. Another hypothesis is that thalamic spots reflect some localized and iron-associated neuropathological alterations. For example, they might be related to small deep infarcts leading to micro-hemorrhages. Such lesions were therefore investigated by neuropathology. Alternative explanations for MR-detected thalamic hypointensities, such as inflammation were also addressed. Finally, the relationship between ferrocyclic calcinosis of the plaques and markers of excitotoxicity was evaluated.

2. Subjects and methods

2.1. Animals

Experiments were conducted on female APP/PS1 transgenic mice overexpressing amyloid precursor (APP) and presenilin 1 (PS1) mutations associated with familial AD (Double Thy1 APP751 SL (Swedish (KM670/671NL) and London (V717I) mutations introduced in the human APP751 sequence) × HMG PS1 M146L transgenic mouse line (Blanchard et al., 2003; Wirths et al., 2001)). In these animals, the amyloid deposition starts at the age of 2.5 months (Blanchard et al., 2003; Wirths et al., 2001). Amyloid-free female PS1 transgenics and wild-type C57BL/6 animals were used as controls.

2.2. MRI evaluation of thalamic hypointense spots and image analysis

Thirty two APP/PS1 (27–103 weeks old) and 36 PS1-amyloid-free mice (27–104 weeks old) were studied using *in vivo* MRI. Eleven mice (7 APP/PS1 and 4 PS1) were followed longitudinally for a period of up to 43 weeks. Post mortem MR imaging was performed in 32 APP/PS1, 26 PS1, and 9 C57BL/6 mice (44–98 weeks old). To address correlations between *in vivo* and post mortem measurements, only mice that underwent two assessments with a maximal in-between

delay of 4 weeks were selected (23 APP/PS1 and 20 PS1 animals).

MRI studies were performed on a 4.7 T Bruker Biospec 47/30 system, equipped with a 12 cm diameter gradient system (200 mT/m). A surface coil (diameter = 30 mm), actively decoupled from the transmitting birdcage probe (Bruker GmbH) was used for signal acquisition.

2.2.1. *In vivo* three-dimensional imaging

For *in vivo* experiments, animals were anesthetized with isoflurane (5% for induction, 1–1.5% for maintenance) in a mixture of N₂ (80%) and O₂ (20%) administered via a facemask. Respiration rate was monitored to insure animal stability until the end of the experiment. Body temperature of the mice was maintained by using water filled heating blanket. For all the mice studied by *in vivo* MRI, images were recorded by using a T2*-weighted (T2*_w) gradient echo (GE) sequence (TR = 47.4 ms, TE = 20 ms, alpha = 15°, spectral width (SW) = 50 kHz, field of view (FOV) = 3 cm × 1.5 cm × 1.5 cm, matrix = 128 × 128 × 128, resolution = 234 μm × 117 μm × 117 μm, signal averaging (NA) = 4, imaging time = 51 min). In addition, for some mice (8 APP/PS1 and 16 PS1 mice), 3D GE images were recorded with a T1-weighted (T1_w) protocol (TR = 25 ms, TE = 2.9 ms, alpha = 30°, SW = 50 kHz, FOV = 3 cm × 1.5 cm × 1.5 cm, matrix = 128 × 128 × 128, resolution = 234 μm × 117 μm × 117 μm, NA = 8, imaging time = 51 min). Three-dimensional T2_w fast spin echo images were also recorded for most of the mice (28 APP/PS1 and 29 PS1 mice) to control for the anatomy of the brain (lack of tumor, for example) (TR = 2500 ms, TE = 14 ms, wTE = 105, RareFactor = 16, SW = 37 kHz, FOV = 3 cm × 1.5 cm × 1.5 cm, matrix = 128 × 128 × 128, resolution = 234 μm × 117 μm × 117 μm, NA = 1, imaging time = 51 min).

2.2.2. Post mortem three-dimensional imaging

After animal death, brains were fixed for at least 1 week in 10% buffered formalin. Then, each brain was put in a small Plexiglass container and embedded in a 2.5% agar gel before being imaged by MRI. Three-dimensional T2*_w GE images were recorded for all brains studied by post mortem MRI (*n* = 32 APP/PS1; *n* = 28 PS1; *n* = 9 C57BL/6 mice; TR = 100 ms, TE = 20 ms, alpha = 15°, SW = 25 kHz, FOV = 1.6 cm × 1.2 cm × 0.75 cm, matrix = 256 × 256 × 128, resolution = 63 μm × 47 μm × 59 μm, NA = 8, imaging time = 7 h). In addition, a 3D T1_w spin echo protocol was also used to record images from some brains (*n* = 23 APP/PS1 and *n* = 14 PS1 mice) (TR = 200 ms, TE = 10 ms, SW = 25 kHz, FOV = 1 cm × 1.5 cm × 0.75 cm, matrix = 128 × 256 × 128, resolution = 78 μm × 58 μm × 58 μm, NA = 1, imaging time = 8 h). T1_w images were not recorded for most of the animals that did not display hypointense thalamic spots on 3D T2*_w image, as after preliminary experiments (see also results), we found that hypointense thalamic spots were

never detected with the T1w protocol without being detected in T2* w images.

2.2.3. MR Images processing: quantification of hypointense spot sizes

The size of the spots detected on the *in vivo* and post mortem 3D T2* w GE were assessed using the Display freeware (available at ftp.bic.mni.mcgill.ca). This freeware allows manual painting of pixels that have intensity below an intensity threshold that can be selected by the user. Then it can automatically count the number of labeled voxels. In our study, the threshold used to consider a voxel as belonging to the thalamic spots was calculated as follows. First a region of interest (ROI) was outlined within the mediadorsal and posterior thalamic nuclei, underneath the fornix bundles, a region located between the typical location of the hypointense thalamic spots (in the vicinity of ventral posteromedial (VPM) thalamic nuclei; see results). The mean (M) and standard deviation (S.D.) of the intensity of the pixels located in this ROI were measured (Image J software). Then the threshold (T) was calculated as ($T = M - 2.576 \times \text{S.D.}$) (2.576 corresponds to a 1% confidence interval for a Gaussian population). The sizes of the hypointense spots were evaluated on the right and left hemispheres, and the values from each hemisphere were summed-up.

2.3. Neuropathology

2.3.1. Tissue processing and histochemical staining

After imaging, the brains from 22 APP/PS1, 22 PS1, and from the five oldest C57BL/6 (92–98 weeks old) mice were processed for histology. They were stored overnight in a solution of 20% glycerin and 2% dimethylsulfoxide (DMSO-G) in 0.1 M phosphate buffer for cryoprotection. Then, they were cut into 40 μm -thick coronal sections on a freezing microtome. One out of eight serial floating sections were rinsed with 0.1 M phosphate buffer and mounted on Superfrost plus glass slides before being processed for Nissl, Congo red, and Perls staining.

2.3.2. Histochemical staining of amyloid plaques

On a first batch of serial sections, ranging from the frontal to the occipital poles, amyloid deposits were labeled by standard Congo red staining (30 min in a 80% ethanol solution saturated with congo red and sodium chloride; adapted from Puchtler et al. (1962)). Slices were observed by means of standard light microscopy and also using a confocal laser-scanning microscope equipped with krypton–argon 488–568 lasers (Bio-Rad Laboratory MRC1024ES, 510 LSM, Zeiss, Germany). Each slice was then digitized using a Super CoolScan 8000 ED high-resolution scanner (Nikon, Champigny sur Marne, France). Regional amyloid load (expressed as percent of tissue surface stained by the Congo red dye) was quantified in the thalamus using computer-based thresholding methods as previously described (Delatour et al., 2006).

2.3.3. Histochemical staining of iron

Iron staining was performed on serial sections using a protocol derived from the standard Perls-DAB method (Nguyen-Legros et al., 1980). Briefly, all reactions were carried out on free floating sections to ameliorate tissue penetration of reagents. Blockade of endogenous peroxidase activity was first done by immersion in a methanol/H₂O₂ solution. Sections were then treated with equal parts of freshly made, aqueous potassium ferrocyanide (2%) and hydrochloric acid (2%) for 20 min. Iron staining was finally intensified using diaminobenzidine (DAB) as chromogen. Brain sections for all PS1 and APP/PS1 mice were simultaneously processed, and incubation in DAB, which was monitored under the microscope to avoid strong background staining, was of the same duration for all animals. After staining, sections were mounted on Superfrost plus slides (Fischer Bioblock Scientific, Illkirch, France), dehydrated and coverslipped for microscopic examination. All slides were digitized as described above. The surface (number of pixels) of iron-positive thalamic spots was manually assessed under Photoshop 6 (Adobe, Paris, France) and overall optical densities from the thalamus were automatically calculated as described previously (El Tannir El Tayara et al., 2006).

2.3.4. Complementary neuropathological examination

Mineralization of thalamic aggregates was evaluated by standard Alizarin red S staining (Mc Gee-Russell, 1958). The efficiency of this method was primarily tested on positive control tissue (canine skin showing calcifications caused by dermatitis) before being applied to mouse brain sections. The vascular architecture in the vicinity of thalamic spots was observed in thionin-stained material and infarcts were subsequently checked on Perls-stained sections. To evaluate levels of inflammation in thalamic areas with or without spots, tomato lectin (*Lycopersicon esculentum*; Vector Laboratories, Burlingame, USA, 1:100) histochemistry was used to identify microglia with standard protocols (Acarin et al., 1994). Finally, to assess local neurodegeneration Fluoro-Jade B staining was performed on brain sections according to standard protocols (Schmued et al., 2000).

2.4. Ultrastructural and analytical characterization

2.4.1. Brain tissue preparation

The 40 μm -thick brain coronal cryo-sections from one mouse with known thalamic pathology (spots/aggregates) were thawed in phosphate buffer, fixed in 4% PAF and 1% glutaraldehyde, and dehydrated in graded series of ethanol before being embedded in Lr-White resin at -20°C for 72 h. Some fragments were post-fixed with OsO₄. Semi-thin sections, 0.5–1.5 μm thick, were obtained with an ultra-microtome and stained with toluidine blue. Selected semi-thin sections 300–400 nm thick and ultra-thin sections 40–60 nm thick were directly collected on silicon plates (for nanoSIMS), copper grids (for ultrastructural

observations) and carbon-plastic covered gold grids (for immunocytochemistry).

2.4.2. Optical and electron microscopic observations

Optical microscopy observations from thalamic regions were first performed from semi-thin sections stained with toluidine blue. Transmission electron microscopic (TEM) studies were performed using analytical 120 or 200 kV TEM on ultra-thin sections unstained or lightly stained with 2% uranyl acetate in water for 30–60 s.

Immunogold localization of β -amyloid was also performed for some sections using primary 4G8 antibody (Sigma, St. Louis, MO, USA). After 30 min incubation with Tris buffer–gelatin (TBG), the sections were floated for 1 h on a drop of primary antibody diluted in TBG (1:100 dilution) at 37 °C. Grids were then incubated in the secondary antibody (IgM conjugated with 10 nm colloidal gold at a dilution of 1:40 (BBInternational Immunogold conjugate EM GOAT F(ab')₂ anti-mouse IgG + IgM:10 nm) for 1 h before being stained with a solution of 2% uranyl acetate for 30–60 s.

2.4.3. NanoSIMS microscopy

Secondary Ion Mass Spectroscopy (SIMS) provides an in situ microanalysis based on the detection of ion species emitted from specimens under the bombardment of energetic primary ions. It allows identification of elements with high specificity and yields high detection sensitivity for chemical analysis even at trace level.

The SIMS instrument used in the present study was a NanoSIMS-50TM ion microprobe (CAMECA, France) equipped with dual primary sources (Cs⁺ or O⁻ beam). Mapping of element distribution was done by scanning the object surface with the tightly focused primary ion beam. Specially

designed for small area analysis, this instrument combines a high spatial resolution (with typical spot size of about 100 nm for Cs⁺ beam and 250 nm for O⁻ beam), high sensitivity, as well as parallel detection capability for the record of up to five different ion species at the same time thus providing element maps with perfect co-localization (Slodzian et al., 1992). Typical NanoSIMS applications in biology have been recently reviewed (Guerquin-Kern et al., 2005).

In the present study, analyses were performed on about 350 nm thick semi-thin sections of embedded material set on clean silicon plates. Using the Cs⁺ beam, maps of CN⁻, P⁻, and S⁻ were recorded. The CN⁻ image reveals the distribution of N in proteins and nucleic acids, which allows the visualization of the morphology of the sample. Ca⁺ and Fe⁺ maps were recorded using the O⁻ beam. Details of the method are provided in Quintana et al. (2006).

3. Results

3.1. MRI-based characterization of the thalamic spots

3.1.1. In vivo images

In vivo 3D GE T2^{*}-w MRI revealed hypointense spots in the thalamus of both APP/PS1 and PS1 mice. These alterations were localized bilaterally in the ventral posterior region of the thalamus (Fig. 1). Spot prevalence was significantly higher in APP/PS1 mice (13 out of 32 mice) as compared to PS1 mice where it involved only 2 animals out of 36 (Fisher's exact test, $p < 0.001$). In addition, in the two PS1 mice showing spots, the lesions were much smaller than in APP/PS1 mice as they measured one and five pixels (0.003 and 0.016 mm³), respectively, versus up to 181 pixels (0.580 mm³) in APP/PS1 mice.

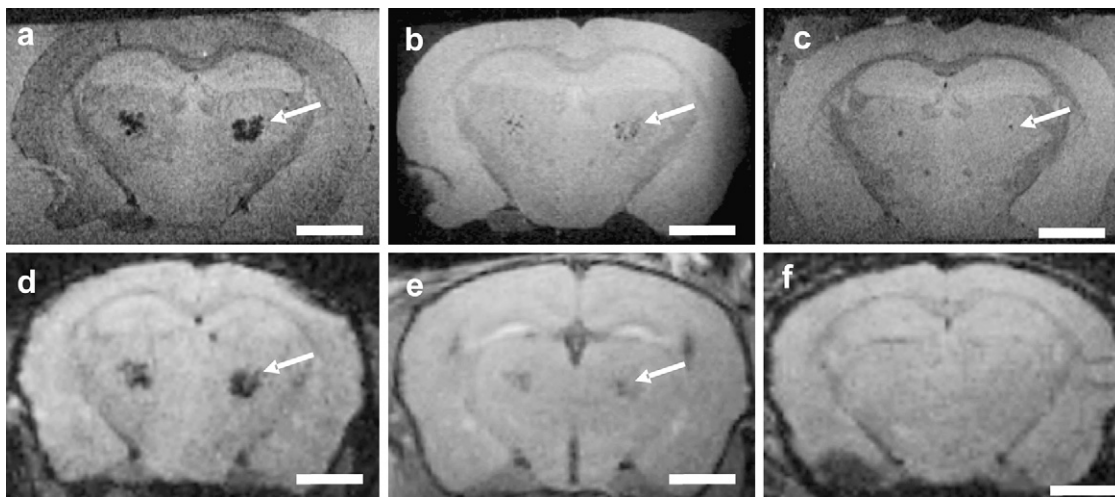


Fig. 1. (a, b, d and e) Hypointense thalamic spots (arrows) in the brain of an APP/PS1 mouse. Spots were larger on T2^{*}w images (a and d: post mortem and *in vivo* images, respectively) than on images recorded with the T1w protocol (b and e: post mortem and *in vivo* images). On the latter images, it is possible to see several distinct aggregates. On T2^{*}w MR images, objects containing iron do appear larger than their actual size. This is related to a so called “susceptibility effect”. Distinct aggregates seen on T1w images had an increased apparent size on the T2^{*}w images and thus appeared as merged objects. (c) Example of thalamic spots in T2^{*}w post mortem images from a PS1 mouse (79 weeks old). (f) The spots could not be detected on *in vivo* T2^{*}w images from the same mouse. Scale bars: 2 mm.

In APP/PS1 mice the spot prevalence did not increase significantly in age groups constituted of animals older than 60 weeks as compared to 27–60 weeks old animals (prevalences of 53 and 33%, respectively; Fisher's test, $p=0.645$, ns). Also, the prevalence of animals with large spots ($>0.3 \text{ mm}^3$) was not significantly increased in old animals group as compared to the 27–60 week animals group (21% versus 0% of the animals, respectively; Fisher's exact test, $p=0.540$, ns). In accordance with the lack of significant increased prevalence of spots/large spots in older APP/PS1 animals, no linear relationship could be found between the age of the animals and the size of the spots either when all animals or only those displaying spots ("spotty mice") were taken into account ($r_s < 0.24$; $p_s > 0.05$). Seven animals were followed longitudinally, but only one of them displayed spots. For this latter animal, an age-related growth of the spots was detected (Fig. 2a).

In *in vivo* MR images from APP/PS1 mice (but not from PS1 mice) recorded with the T1w protocol, the spots were also visible but with a smaller size when compared to T2* w images (Fig. 1). Spot detection in the so called T1w protocol was due to a residual T2* effect.

3.1.2. Post mortem images

Post mortem T2* w GE images confirmed the occurrence of hypointense spots in the thalamus of a subpopulation of APP/PS1 and PS1 mice (Fig. 1). Spots were also detected in old C57BL/6 mice (Fig. 2b). Spots prevalence was higher in young (29–60 weeks) APP/PS1 mice as compared to young PS1 mice (63% of APP/PS1 mice diagnosed with spots versus 0% of PS1 animals; Fisher's test, $p < 0.5$). On the other hand, spots prevalence was similar in older (>60 weeks) transgenics (79% of the old APP/PS1 mice diagnosed with spots versus 58% of the PS1 animals; Fisher's test, $p = 0.186$). Spots were however larger in aged APP/PS1 mice as compared to PS1 or C57BL/6 animals (Fig. 2b and c). Hence, the percentage of animals with spots larger than 0.3 mm^3 was significantly higher in aged APP/PS1 as compared to PS1 mice (Fisher's test, $p < 0.05$) and the nine mice with the biggest spots were from the APP/PS1 genotype group (Fig. 2b). Due to the small number of animals, no statistical analysis could be performed to compare C57BL/6 animals and other strains, but the size of the detected spots in these animals was similar to that detected in PS1 animals.

In APP/PS1 animals, as for *in vivo* images, the prevalence of the spots was not significantly increased in older animals as compared to younger mice (Fisher's test, $p = 0.378$, ns) (Fig. 2c) and the size of the spots measured on T2* w images were not correlated to the age of the animals ($r = 0.34$; $p = 0.056$). On the other side, in PS1 mice the prevalence of the spots occurrence was increased in older animals as compared to younger mice (Fisher's test, $p < 0.05$). Also, in the PS1 genotype, the size of the spots was significantly correlated to the age of the animals ($r = 0.48$; $p < 0.05$). Old C57BL/6 mice also seemed to develop more spots than younger wild-type mice as none of the four 44 weeks old mice

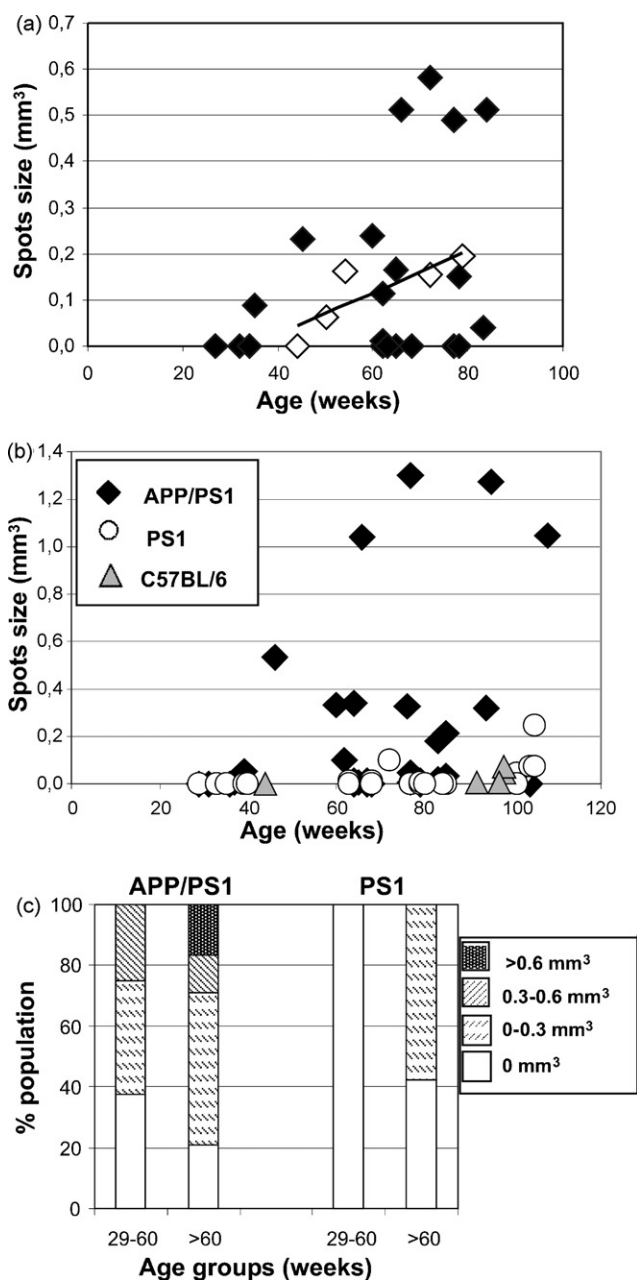


Fig. 2. (a) Size of the thalamic spots measured in *in vivo* images from APP/PS1 mice as a function of age. Dark lozenges represent animals from transversal studies. Seven animals were followed-up longitudinally and only one of them (white lozenges) had spots. The line represents the linear regression curve fitting the size of the spots to the age of this animal. (b) Size of the thalamic spots measured in post mortem images from APP/PS1, PS1 and C57BL/6 mice (for the C57BL/6 mice, the triangle symbol at 44 weeks correspond to four mice that did not show thalamic spots). (c) Prevalence of thalamic spots of various sizes in adult and old APP/PS1 ($n=8$ and 24, respectively) and PS1 ($n=7$ and 19, respectively) mice.

that we investigated had spots and five out of five 92–98 week mice investigated displayed spots (mean size = 0.029 mm^3 ; size range = $0.005-0.073 \text{ mm}^3$).

On the post mortem images recorded with the T1w protocol, hypointense structures could also be detected in the

thalamus of animals that displayed spots on T2* w images. These hypointense alterations appeared as disseminated small aggregates rather than large globular structures as seen on T2* w images (Fig. 1).

Comparison of the size of the spots detected in *in vivo* and post mortem T2* w images revealed a good correlation for APP/PS1 mice ($r=0.96$, $p<0.001$). For these animals, the equation of the curve fitting the size of the post mortem and *in vivo* spots was $y=2.262x-0.02$, which means that the size of the hypointense regions on T2* w post mortem images were more than two times larger than that of the spots on *in vivo* images. This may be explained by the slightly different sequence parameters used for the image recording. For PS1 mice, no significant correlation was found between the size of the spots measured in *in vivo* and post mortem images ($p>0.05$). This could be explained by the reduced number of live PS1 mice diagnosed with spots (only two animals), probably because the size of the spots in PS1 mice was below the threshold of *in vivo* detectability.

3.2. In APP/PS1, but not in PS1 or C57BL/6 mice, thalamic spots are matched with amyloid deposits containing mineralized ferro-calcic aggregates

Dense clusters of iron-positive structures (Fig. 3) were observed in the ventral posteromedial and posterior thalamic nuclei (VPM and Po) of 15 out of the 17 APP/PS1 mice diagnosed with post mortem MRI spots and subsequently processed for histology. Such lesions were never detected in animals that did not show spots on MR images. In addition, a strong positive correlation was obtained between the size of MRI spots in APP/PS1 mice (evaluated *in vivo* or *ex vivo*) and density of Perls-stained deposits (Table 1). Finally, registration of MR images and histological section with Perls-positive structures underlined a high level of co-localization, reinforcing the contention that hypointense zones detected by MRI are indeed thalamic iron deposits (Fig. 3a and b).

On the other side, in PS1 mice showing thalamic MRI spots, we could detect iron deposits in only two animals (Fig. 3f). This may be explained by the small size of the lesions in PS1 mice, which makes them difficult to localize them on 40 μm -thick serial histological sections (sampling bias). In C57BL/6 mice, iron deposits were also found in only two out of the five animals in which hypointense spots were detected on post mortem MR images.

In APP/PS1 mice, Perls-DAB stainings also showed discrete accumulation of iron in isocortical and hippocampal plaques (see left inset of Fig. 3b). PS1 (left inset, Fig. 3f) or C57BL/6, plaques-free, mice were devoided of such labeling.

On thionin-stained sections from APP/PS1 (but not from PS1) mice with hypointense thalamic spots in *in vivo* and/or post mortem MRI, the Perls-positive deposits appeared as dense-cored structures surrounded by microglial cells (Fig. 3e), reminiscent of inflammatory reaction generally seen in the vicinity of amyloid plaques. The location of iron deposits in the core of A β plaques was definitively confirmed by double (Congo red/Perls-DAB) staining (Fig. 3c). The morphology of Congo red-stained objects surrounding Perls-positive aggregates was further examined by means of confocal laser-scanning microscopy and corroborated iron precipitates within amyloid plaques (Fig. 3d). Concerning PS1 mice neurohistological examination from Congo red-stained sections did not reveal, as expected, any amyloid deposits.

Toluidine blue stained semi-thin sections from APP/PS1 mice with spots showed thalamic plaques of variable sizes (5–100 μm) presenting different levels of staining (classified as weak, heterogeneous, and intense) (Figs. 3g and 5). Weakly stained plaques analyzed with electron microscopy occasionally displayed sparse mineral structures (Fig. 4a and b) while plaques classified as heterogeneously stained with toluidine blue were invariably constituted of A β fibrils intermingled with mineralized structures that did not show A β immunoreactivity (Fig. 4c and e). Finally deposits with intense toluidine blue staining had an electron dense mineralized core with concentric layers surrounded by amyloid fibers (Fig. 4f). NanoSIMS maps revealed the distribution of CN $^-$, S $^-$, P $^-$, Ca $^+$ and Fe $^+$ within the toluidine blue labeled regions from heterogeneous deposits and from the intense deposits (Fig. 5). The CN $^-$ and S $^-$ nanoSIMS emission correspond to proteins or peptides (such as A β) and the high P $^-$, Ca $^+$ and Fe $^+$ emission to mineralized phase. These results suggest that a mineralization process occurs within the thalamic amyloid plaques. The sparse mineral structures detected in amyloid plaques by TEM might be an early stage of the mineralization process while the strongly toluidine blue stained structures showing concentric layers on TEM images could represent the later stages of plaque mineralization.

Calcium deposition within thalamic plaques was confirmed by histochemical staining of 40 μm sections with Alizarin red S. Notably, Alizarin red staining was also

Table 1

Correlation between the size of the spots in APP/PS1 mice (evaluated from *in vivo* and post mortem MRI) with different histological measurements: size of the aggregates, thalamic amyloid and iron loads

	Spots size <i>in vivo</i>	Spots size post mortem	Aggregates size (iron stain)
Spots size <i>in vivo</i>	N/A	$r=0.956$; $p<0.001$	$r=0.973$; $p<0.001$
Spots size post mortem	$r=0.956$; $p<0.001$	N/A	$r=0.937$; $p<0.001$
Thalamic amyloid load	NS	$r=0.431$; $p<0.05$	$r=0.406$; $p=0.061$
Thalamic iron load	NS	NS	NS
Thalamic iron load (without including aggregates)	NS	NS	NS

NS: non-significant ($p>0.5$); N/A: non-relevant measure.

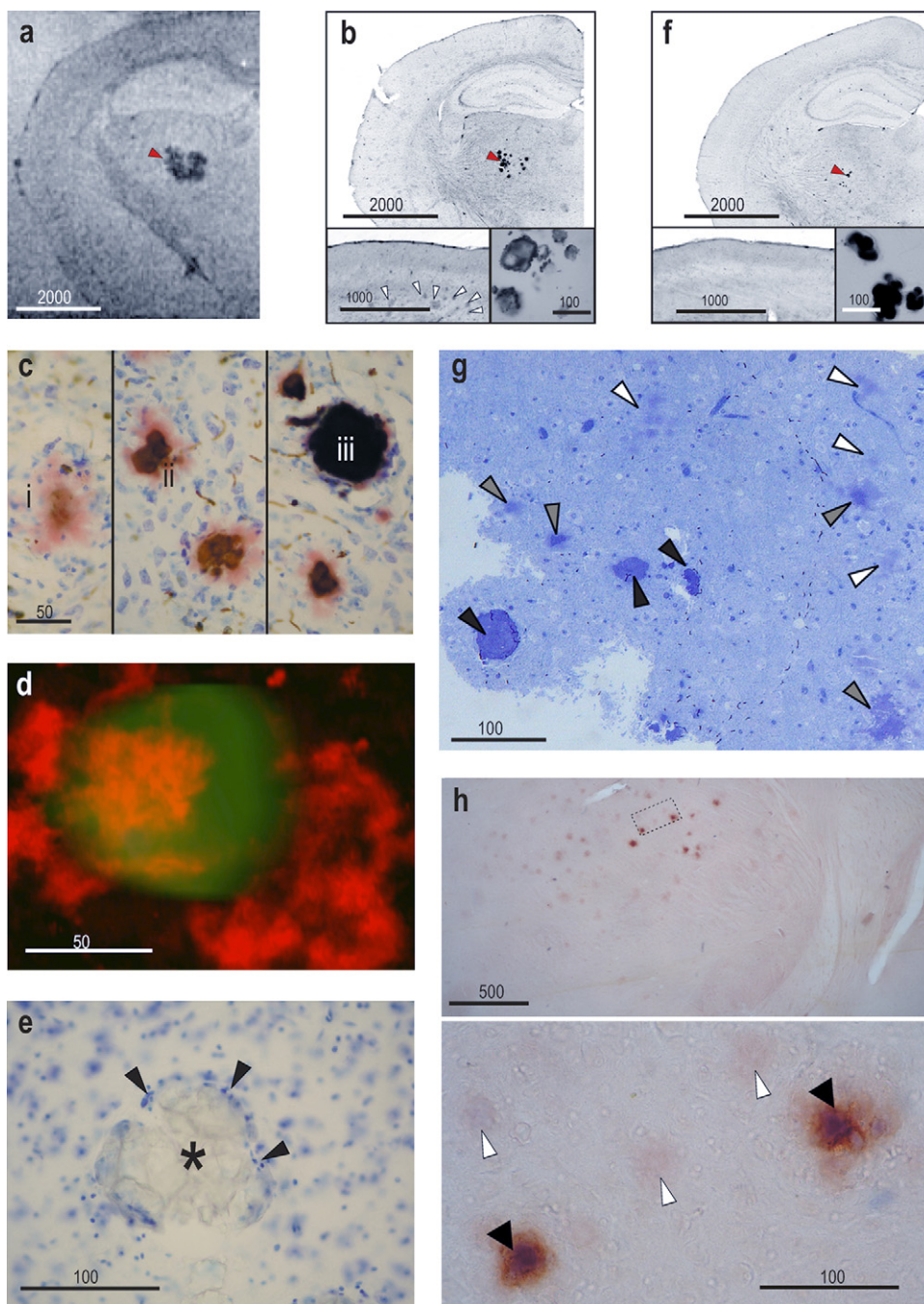


Fig. 3. Co-localization of hypointense spots on MR images from an APP/PS1 mouse (a) and Perls-DAB positive (b) structures. In (b), right inset shows the Perls-positive aggregates at high magnification; left inset illustrates (weak) iron deposition in the cortex associated with amyloid plaques (arrow heads). (c) Double (Congo red/Perls-DAB) stainings showing Perls-positive iron aggregates within amyloid plaques. Different levels of iron deposits are visible in various plaques: plaques with sparse iron staining (i) and plaques with medium to high densities (ii and iii) iron deposits. (d) Confocal microscopic image showing Congo red-stained amyloid substance (red) surrounding an iron core (green; extrapolated and reconstructed from images taken under white light illumination). (e) Thionin section showing crystalline aggregate (*) surrounded by microglial cells (arrowheads). (f) Perls-DAB positive structures in the thalamus from PS1 mice; right inset shows the stained globular structures at higher magnification (same small-size iron aggregates were also observed in old non-transgenic C57BL/6 mice); left inset shows no significant iron deposits in the cortical ribbon. (g) Toluidine blue stained semi-thin section of the thalamus of an APP/PS1 mouse showing deposits of variable sizes (5–100 μm) with different levels of staining: weak staining (white arrowheads), heterogeneous staining (gray arrowheads) and intense staining (black arrowheads). (h) Alizarin red staining in an APP/PS1 mouse that displayed hypointense spots on MRI images. Most of amyloid deposits showed weak labeling (white arrowheads) while thalamic plaques containing aggregates displayed intense staining (black arrowheads). All scale bars are in micrometers. (For interpretation of the references to color in this figure legend, the reader is referred to the web version of the article.)

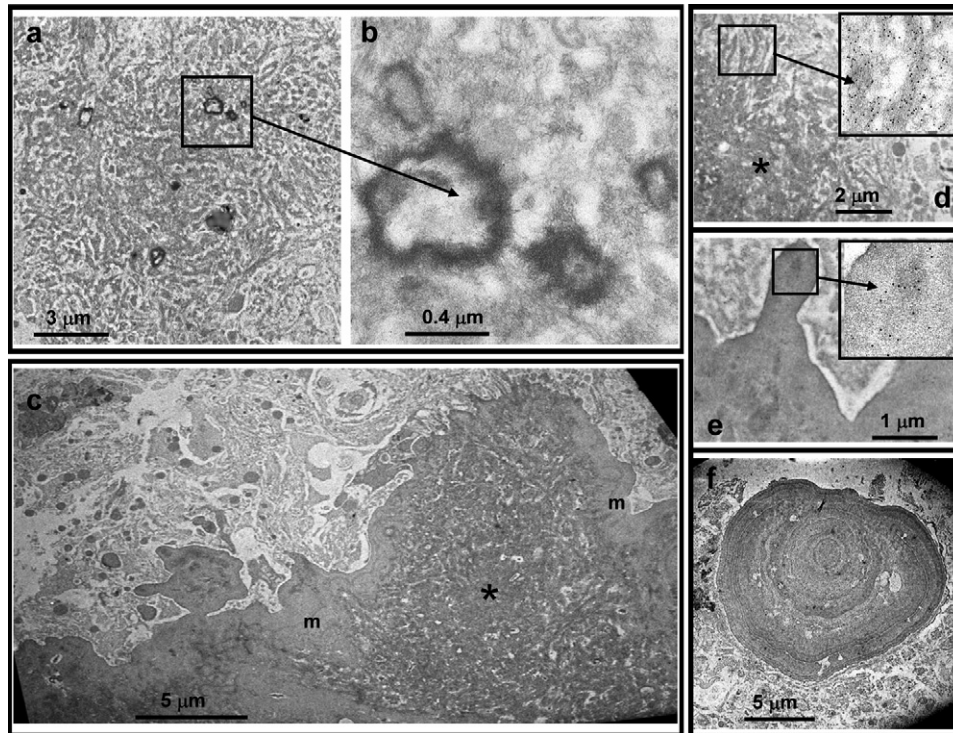


Fig. 4. TEM images of amyloid deposits. (a) Amyloid deposit with sparse mineralized structures (seen at higher magnification in b). (c) Illustration of another stage of the mineralization process where mineralized regions (m) surrounds amyloid deposits (*). TEM images after immunolabeling with anti-A β antibodies coupled with colloidal gold were used to determine the extent of amyloid plaques (* on image d) and showed that the A β peptide was not immunodetected in smooth mineralized regions (e). In d and e, the insets correspond to a magnification of the outlined frame and show colloidal gold particles labeling the amyloid plaque. (f) Dense mineralized aggregates detected in APP/PS1 mice corresponding to an end-stage pathological process.

detected in isocortical and hippocampal plaques of APP/PS1 mice and in thalamic plaques from animals without aggregates. However, the staining was much stronger in thalamic plaques containing aggregates than in other amyloid deposits (Fig. 3h).

3.3. Relationship between thalamic aggregates and histological markers of brain alterations ?

3.3.1. Relationship with overall A β deposition

The highest prevalence of spots in APP/PS1 mice as compared to PS1 (or C57BL/6) animals suggested that amyloid pathology favors the occurrence of such lesions. In addition, correlative studies in APP/PS1 mice revealed a statistically significant positive correlation between the size of the spots assessed from high-resolution post mortem images and the thalamic amyloid load (Table 1). There was also a trend for a linear positive correlation between the density of thalamic iron-positive aggregates detected histologically and the local amyloid load (Table 1). The size of the spots measured with *in vivo* MRI did not however correlate with the thalamic amyloid load. This might be explained by the lower resolution of *in vivo* MRI as compared to post mortem MRI but concurrently by a somehow poor linear relationship between plaque burden and MRI hypointensities.

3.3.2. Relationship with cerebral iron deposition and distribution

Correlational analysis was also carried out to determine the relationship between local iron aggregates in thalamic nuclei and the overall distribution of iron within this brain structure. This analysis was only performed in APP/PS1 mice (as only two PS1 and two C57BL/6 mice showed Perls-positive aggregates) and showed no correlation between the size of aggregates (determined by iron staining) and Perls optical density of the whole thalamus (Table 1). Also the density of spots assessed by *in vivo* or post mortem MRI did not correlate with Perls thalamic optical density (Table 1), indicating that iron levels in this brain region was not linked to the occurrence or lack of spots/aggregates.

3.3.3. Relationship with vascular impairments

Post mortem histological analysis did not show any vascular impairment in mice displaying thalamic aggregates. First, no histological signs evocative of thalamic infarcts could be detected, neither on thionin nor on Perls-stained sections although small extra-thalamic infarcts were occasionally observed (Fig. 6). In addition, blood vessels examined in Nissl-stained sections (by increasing depth of field of microscopical images) showed no obvious anomalies in vascular architecture in the vicinity of the thalamic spots in APP/PS1 mice.

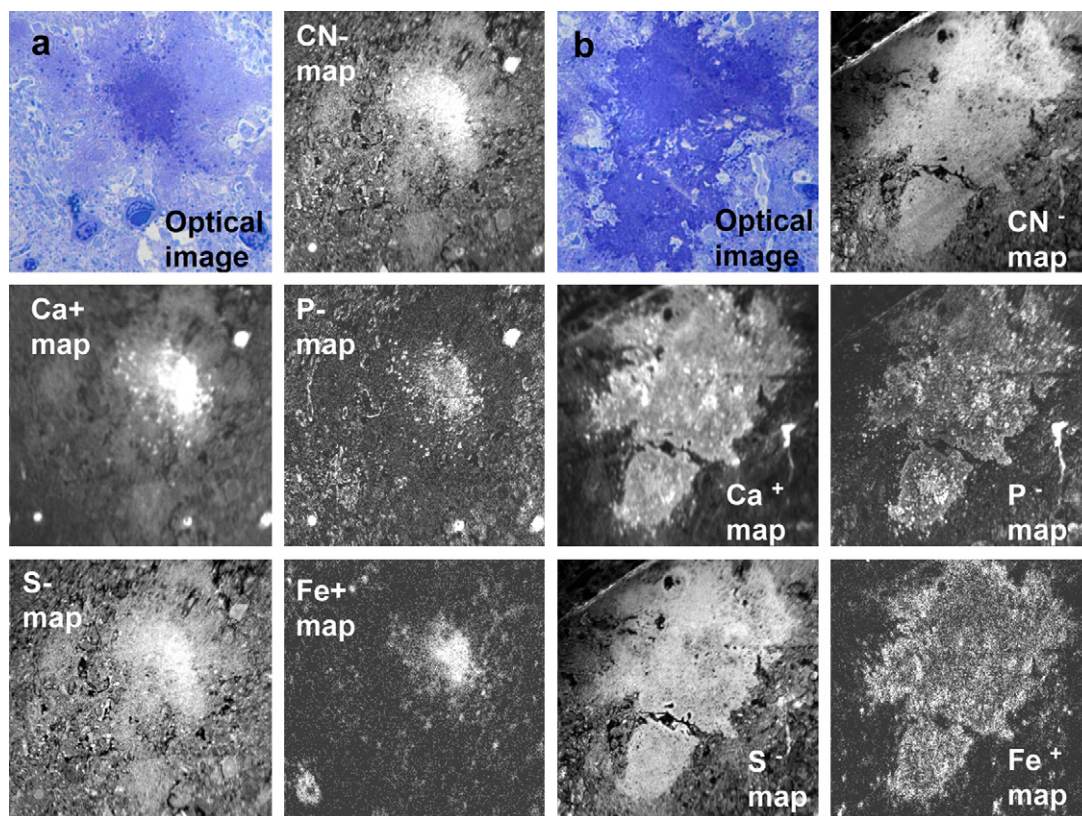


Fig. 5. Optical and NanoSIMS analytical images of partially (a) and densely mineralized (b) plaques. Toluidine blue and CN^- images show the morphology of the plaques. The distribution of calcium, phosphor, sulfur and iron in the plaques are shown on other frames. On a and b, image frames measure $65\ \mu\text{m} \times 65\ \mu\text{m}$ and $55\ \mu\text{m} \times 55\ \mu\text{m}$, respectively.

3.3.4. Relationship with inflammation and neurodegeneration

Lectin histochemistry showed no inflammation in PS1 mice. On the contrary, a heavy inflammatory reaction was observed in APP/PS1 animals, with all amyloid plaques being associated with peripheral reactive microglia. There was no qualitative difference in levels of inflammation between

plaques with or without iron aggregates, in the thalamic and extra-thalamic regions (Fig. 7a and b).

The Fluoro-Jade dye remarkably stained the core of amyloid deposits and degenerating dystrophic neurites from APP/PS1 mice (Fig. 7c–f). No neuronal labeling was noted but star-shaped cells with the reminiscent morphology of astrocytes showed evidence of positive staining. There was no staining difference between APP/PS1 mice lacking aggregates and mice developing these lesions. In particular no evidence of neuronal degeneration was observed in the periphery of thalamic aggregates.

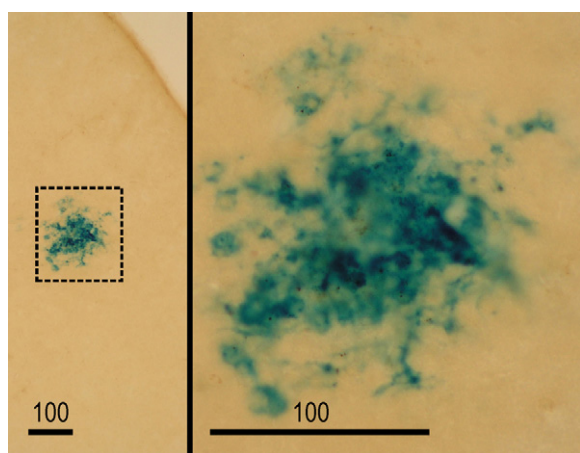


Fig. 6. Evaluation of vascular anomalies in APP/PS1 mice. Cortical infarcts such as those displayed on the figure were occasionally detected in the brain of APP/PS1 mice (Perls stain). Thalamic infarcts were never observed in animals displaying aggregates. Scale bars are in micrometers.

4. Discussion

4.1. General characterization of thalamic spots in APP/PS1, PS1, and C57BL/6 mice

MR images recorded in a large cohort of APP/PS1, PS1, and C57BL/6 mice studied at different ages allowed detecting hypointense thalamic spots. Previous MRI studies (Jack et al., 2004; Vanhoutte et al., 2005) reported similar brain anomalies in APP or APP/PS1 mice, but, to our knowledge, not in wild type or PS1 control mice. In our study, the prevalence and size of the spots was however higher in APP/PS1 as compared to control (PS1, C57BL/6) mice, which suggests that amyloid-

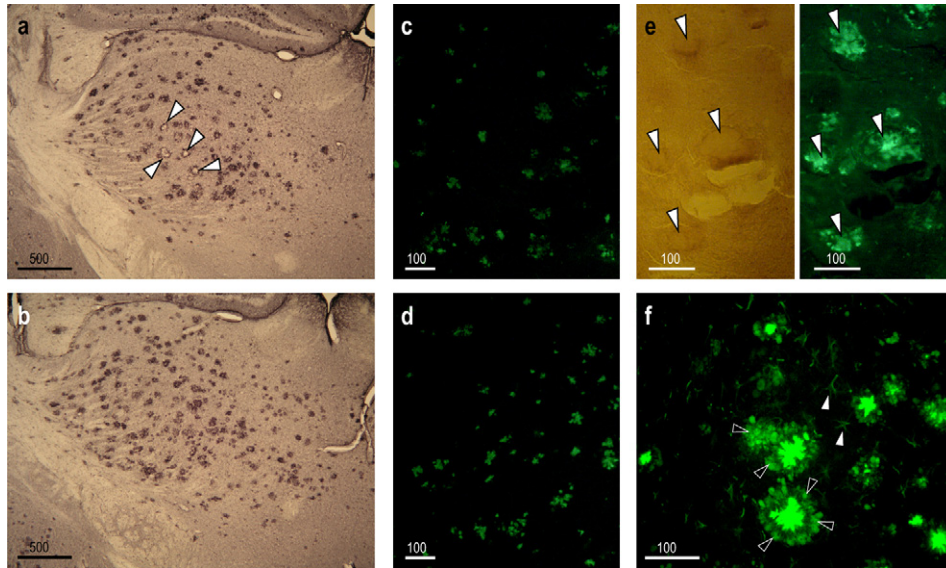


Fig. 7. (a and b) Lectin histochemistry showing heavy inflammatory reaction surrounding amyloid deposits in APP/PS1 animals. Inflammation process surrounded the thalamic aggregates (arrows) but was not increased in mice with aggregates (a) compared with animals without thalamic aggregates (b). (c–f) Fluoro-Jade B stained the core of thalamic amyloid deposits of APP/PS1 mice with (c) or without (d) aggregates. (e) Plaques containing aggregates (arrowheads) were also positive for Fluoro-Jade; no degenerated neurons were observed in the vicinity of thalamic aggregates. (f) Fluoro-Jade also stained star-shaped cells with the reminiscent morphology of astrocytes (white arrowheads) and dystrophic neurites (black arrowheads) in all APP/PS1 mice.

dosis favors the occurrence of such MRI detectable lesions. In PS1 and C57BL/6 mice, we showed that the prevalence and size of the lesions was age dependent. On the other side, in APP/PS1, even if some trend was visible, the prevalence and size of the lesions were not significantly increased with aging.

In APP/PS1 mice, the MRI-detected spots were caused by parenchymal mineral structures, composed of iron and various minerals such as calcium or phosphorus, co-localized with amyloid deposits. On the other side, in PS1 or C57BL/6 mice, the spots were related to discrete small-size iron deposits in the absence of amyloid plaques. The presence of iron aggregates in the thalamus of very old wild-type mice has already been described in other studies (Fraser, 1968). All these observations suggest that such alterations are not specifically related to the PS1 transgene, but are mainly a characteristic of aged normal mice.

4.2. High level of ferro-calcification of thalamic amyloid plaques as compared to other plaques is responsible for their better detection on MR images

In a second part of the study, we focused on the fine characterization of the ferro-calcification process occurring in the thalamic MRI detectable plaques from APP/PS1 mice. Histological, TEM and microanalysis studies showed different stages of iron deposition and calcifications within the thalamic amyloid deposits. In fact several forms of iron deposits ranging from sparse punctuated deposits to dense-core globular aggregates were detected. Regarding calcification, some amyloid deposits displayed sparse calcification, others presented more severe mineralization involving the center or

the periphery of the plaques and, finally, massive mineral aggregates were detected in some plaques.

We also showed that amyloid plaques from other brain regions (e.g. isocortex, hippocampus) were stained for iron and calcium, although with a much reduced intensity than the thalamic plaques. Iron deposition within amyloid plaques has already been reported in transgenic mice (El Tannir El Tayara et al., 2006; Falangola et al., 2005) as well as in humans (LeVine, 1997; Thompson et al., 2001). Calcium deposition within plaques has also been described in humans (Watt, 1996). This suggests that ferro-calcic deposition is a common process occurring in most plaques both in animals and humans. This deposition is however relatively mild in isocortical and hippocampal plaques as compared to what occurs in the thalamic plaques of transgenic mice. The high dense ferro-calcic deposition observed in thalamic plaques might thus be considered as an amplified end-product resulting from a general process that occurs in all amyloid plaques. This process is of interest because it modifies the NMR properties of the plaques and makes them easily detectable by *in vivo* MRI without contrast agent.

Previous studies at higher magnetic field have shown that isocortical and hippocampal plaques can also be detected by MRI without contrast agents (Braakman et al., 2006; Jack et al., 2004; Lee et al., 2004; Vanhoutte et al., 2005). In our experimental conditions, isocortical and hippocampal plaques were not detected. This is probably only related to the relatively low magnetic field that we used as compared to other studies. More interestingly, the studies that were able to detect plaques in the whole brain by MRI without contrast agents showed that all the plaques could not be detected and a recent report suggested that iron depositions within the

plaques is a critical event making plaque detection possible. One can expect that mechanisms involved in iron deposition within the isocortical and hippocampal plaques are the same as the one that occurred, although amplified, for the thalamic plaques.

One important difference between the thalamic plaques and isocortical/hippocampal plaques detected by MRI in previous studies is that, as shown in our study, the thalamic lesions detected by *in vivo* MRI are not correlated to (thus not very representative of) the brain amyloidosis. The facilitated detection of these lesions by MRI even at relatively low field thus does not seem to be usable to assess amyloid loads. Conversely, hippocampal and isocortical plaques detected on *in vivo* and *ex vivo* MRI without contrast agent are correlated with the amyloid load (Jack et al., 2005). It is therefore tempting to conclude that extra-thalamic plaques are a better target for relevant biomarker investigations than easily MRI-detectable thalamic plaques.

4.3. The stress hypothesis

Several hypothesis were evaluated to explain the high ferro-calcification of amyloid plaques in APP/PS1 mice. It might be tempting to posit ischemic or excitotoxic events in the thalamus of our APP/PS1 mice as promoting increased local calcium aggregation and its association with amyloid deposits. Indeed, reports from the literature suggest that hypoxic/ischemic alterations can lead to mineralization in the central nervous system including the thalamus (Kato et al., 1995). Such process might be worsened in APP transgenic mice as they have increased vulnerability to brain ischemia (Koistinaho et al., 2002; Sadowski et al., 2004). Also several reports from experimental studies in animals suggest a critical role of excitotoxicity in the genesis of calcified deposits (Gayoso et al., 2003; Mahy et al., 1995; Petegnief et al., 1999; Rodriguez et al., 2000; Stewart et al., 1995). Hence excitotoxic lesions induced by stereotaxic microinjection of glutamate agonists can modify calcium homeostasis and are associated with massive intracellular Ca^{2+} increase leading to its precipitation (Rodriguez et al., 2000). However, in our study, histological examination did not reveal any sign of local excitotoxic background around thalamic aggregates. First, no necrotic/picnotic neurons were observed around ferro-calcic deposits (data not shown). Also Fluoro-Jade B staining did not reveal local degeneration associated with thalamic aggregates: star-shaped cells (presumably astrocytes) were stained by the dye as already described in primates and AD patients (Colombo and Puissant, 2002) as well as in transgenic mice with brain amyloidosis (Damjanac et al., 2007) but no degenerating neurons were found, neither in the VPM/Po thalamic nuclei nor in other brain areas. Dystrophic enlarged neurites forming the crown of senile plaques also showed positive Fluoro-Jade staining. These observations fit well with the generally accepted assumption that transgenic mice modeling AD's brain amyloidosis do not develop overt neurodegeneration (Delatour, *in press*). In

addition there was no exacerbated inflammation around the mineralized plaques compared to other plaques with almost all A β deposits being associated with strong microgliosis. Finally we did not detect any neuropathological evidence of microinfarcts or vascular alterations. Also, no obvious cell loss or ischemia-related pathology was noted in the vicinity of thalamic aggregates. These observations contradict the hypothesis that excitotoxic/inflammatory/vascular/hypoxic alterations are responsible for mineralized lesions associated with the MRI spots in APP/PS1 mice. In addition, neurological and cognitive evaluation of APP_{SL} mice (another transgenic line in which we detected hypointense thalamic spots caused by local iron clustering) did not highlight any relationship between the presence of aggregates and behavioral impairments (data not shown).

4.4. The biofloculant hypothesis

Alternative hypothesis can be provided to explain increased ferro-calcic aggregation in the amyloid plaques from the thalamus. The association between iron and A β is in keeping with the fact that A β is a metalloprotein with known binding sites for metal ions at histidine and tyrosine residues. The local presence of biometals such as iron in plaques could be explained by the sequestration function of A β deposits directed against extracellular potentially neurotoxic solutes (Robinson and Bishop, 2002). The overall thalamic iron pool does not seem however to be directly responsible for the formation of iron containing aggregates as we noticed no relationship between spots prevalence and iron level in the entire thalamus. Furthermore, by post mortem MRI, we showed that iron-associated spots occurred in VPM/Po nuclei of 58% of the old PS1 animals and in all the old evaluated C57BL/6 mice. This suggests that VPM/Po nuclei are prone to iron accumulation even in aged amyloid-free mice. In APP/PS1, such iron is probably trapped within the plaques lesions. Concerning the association between calcium and amyloid, it is known that calcification processes require a matrix on which calcium and other minerals are trapped and amyloid proteins may serve as such matrix (Reinus et al., 1993; Sano et al., 1990).

5. Conclusion

To conclude, MRI detectable thalamic spots are recently discovered A β -associated lesions, reported at least in four different transgenic lines (Jack et al., 2004; Vanhoutte et al., 2005, present study, APP_{SL} monogenic model: unpublished observations). They are late and somehow “distant” markers of brain amyloidosis that are associated with ferrocalcinosis of the amyloid deposits. Such lesions are presumably related to an amplified process that also occurs, with less intensity, in amyloid plaques from other brain regions such as the isocortex or the hippocampus. These lesions might be related to the ability of amyloid plaques to capture a large

amount of iron and calcium. While our data do not suggest direct relationship between brain stress or neurodegeneration and thalamic ferrocalfinosis, it remains unclear whether iron-calcium aggregates mediate toxicity or represent a compensatory neuronal protective mechanism in old animals and in mice developing brain amyloidosis.

Disclosure statement

Marc Dhenain: none; Nadine El Tannir El Tayara: none; Ting-Di Wu: none; Maryvonne Guégan: none; Andreas Volk: none; Carmen Quintana: none; Benoît Delatour: funding received from Sanofi-Aventis Neurodegenerative Disease Group.

Acknowledgements

We thank the Sanofi-Aventis Neurodegenerative Disease Group for the generous gift of the animals involved in this study. This work was supported by the Aging ATC 2002 (INSERM), the Fédération pour la Recherche sur le Cerveau 2003, the Del Duca Foundation, the ACI Neurosciences 2004 (French Research Department), the Ministerio de Educación, Cultura y Deporte (Spain) (grant PR2002-0261), and grant BMC2002-00996 from the Dirección General de Investigación (Spain). We are grateful to R. Arranz and C. Patiño for helpful assistance in immunocytochemical studies and to Dr. S. Davis for carefully reading and correcting the manuscript.

References

- Acarin, L., Vela, J.M., Gonzalez, B., Castellano, B., 1994. Demonstration of poly-N-acetyl lactosamine residues in amoeboid and ramified microglial cells in rat brain by tomato lectin binding. *J. Histochem. Cytochem.* 42 (8), 1033–1041.
- Blanchard, V., Moussaoui, S., Czech, C., Touchet, N., Bonici, B., Planche, M., Canton, T., Jedidi, I., Gohin, M., Wirths, O., Bayer, T.A., Langui, D., Duyckaerts, C., Tremp, G., Pradier, L., 2003. Time sequence of maturation of dystrophic neurites associated with Ab deposits in APP/PS1 transgenic mice. *Exp. Neurol.* 184 (1), 247–263.
- Braakman, N., Matsysik, J., van Duinen, S.G., Verbeek, F., Schliebs, R., de Groot, H.J., Alia, A., 2006. Longitudinal assessment of Alzheimer's beta-amyloid plaque development in transgenic mice monitored by in vivo magnetic resonance microimaging. *J. Magn. Reson. Imaging.*
- Colombo, J.A., Puissant, V.I., 2002. Fluoro Jade stains early and reactive astroglia in the primate cerebral cortex. *J. Histochem. Cytochem.* 50 (8), 1135–1137.
- Damjanac, M., Bilan, A.R., Barrier, L., Pontcharraud, R., Anne, C., Hugon, J., Page, G., 2007. Fluoro-Jade((R)) B staining as useful tool to identify activated microglia and astrocytes in a mouse transgenic model of Alzheimer's disease. *Brain Res.* 1128 (1), 40–49.
- Delatour, B., Guegan, M., Volk, A., Dhenain, M., 2006. In vivo MRI and histological evaluation of brain atrophy in APP/PS1 transgenic mice. *Neurobiol. Aging* 27 (6), 835–847.
- Delatour, B., Le Cudennec, C., El Tannir-El Tayara N., Dhenain M., in press. Transgenic models of Alzheimer's pathology: Success and caveat. In: Welsh, E.M. (Ed.). *Topics in Alzheimer's Disease*. Nova Publishers.
- El Tannir El Tayara, N., Delatour, B., Le Cudennec, C., Guegan, M., Volk, A., Dhenain, M., 2006. Age-related evolution of amyloid burden, iron load, and MR relaxation times in a transgenic mouse model of Alzheimer's disease. *Neurobiol. Dis.* 22 (1), 199–208.
- Falangola, M.F., Lee, S.P., Nixon, R.A., Duff, K., Helpert, J.A., 2005. Histological co-localization of iron in Abeta plaques of PS/APP transgenic mice. *Neurochem. Res.* 30 (2), 201–205.
- Fraser, H., 1968. Bilateral thalamic calcification in ageing mice. *J. Pathol. Bacteriol.* 96 (1), 220–222.
- Gayoso, M.J., Al-Majdalawi, A., Garrosa, M., Calvo, B., Diaz-Flores, L., 2003. Selective calcification of rat brain lesions caused by systemic administration of kainic acid. *Histol. Histopathol.* 18 (3), 855–869.
- Guerquin-Kern, J.L., Wu, T.D., Quintana, C., Croisy, A., 2005. Progress in analytical imaging of the cell by dynamic secondary ion mass spectrometry (SIMS microscopy). *Biochim. Biophys. Acta* 1724 (3), 228–238.
- Jack Jr., C.R., Garwood, M., Wengenack, T.M., Borowski, B., Curran, G.L., Lin, J., Adriany, G., Grohn, O.H., Grimm, R., Poduslo, J.F., 2004. In vivo visualization of Alzheimer's amyloid plaques by magnetic resonance imaging in transgenic mice without a contrast agent. *Magn. Reson. Med.* 52 (6), 1263–1271.
- Jack Jr., C.R., Wengenack, T.M., Reyes, D.A., Garwood, M., Curran, G.L., Borowski, B.J., Lin, J., Preboske, G.M., Holasek, S.S., Adriany, G., Poduslo, J.F., 2005. In vivo magnetic resonance microimaging of individual amyloid plaques in Alzheimer's transgenic mice. *J. Neurosci.* 25 (43), 10041–10048.
- Kato, H., Araki, T., Itoyama, Y., Kogure, K., 1995. Calcium deposits in the thalamus following repeated cerebral ischemia and long-term survival in the gerbil. *Brain Res. Bull.* 38 (1), 25–30.
- Koistinaho, M., Kettunen, M.I., Goldsteins, G., Keinanen, R., Salminen, A., Ort, M., Bures, J., Liu, D., Kauppinen, R.A., Higgins, L.S., Koistinaho, J., 2002. Beta-amyloid precursor protein transgenic mice that harbor diffuse A beta deposits but do not form plaques show increased ischemic vulnerability: role of inflammation. *Proc. Natl. Acad. Sci. U.S.A.* 99 (3), 1610–1615.
- Lee, S.P., Falangola, M.F., Nixon, R.A., Duff, K., Helpert, J.A., 2004. Visualization of beta-Amyloid plaques in a transgenic mouse model of Alzheimer's disease using MR microscopy without contrast reagents. *Magn. Reson. Med.* 52, 538–544.
- LeVine, S.M., 1997. Iron deposits in multiple sclerosis and Alzheimer's disease brains. *Brain Res.* 760 (1–2), 298–303.
- Mahy, N., Bendahan, G., Boatell, M.L., Bjelke, B., Tinner, B., Olson, L., Fuxe, K., 1995. Differential brain area vulnerability to long-term subcortical excitotoxic lesions. *Neuroscience* 65 (1), 15–25.
- Mc Gee-Russell, S.M., 1958. Histochemical methods for calcium. *J. Histochem. Cytochem.* 6 (1), 22–42.
- Nguyen-Legros, J., Bizot, J., Bolesse, M., Pulicani, J.-P., 1980. "Noir de diaminobenzidine": une nouvelle méthode histochimique de révélation du fer exogène ("Diaminobenzidine black"): a new histochemical method for the visualization of exogenous iron. *Histochemistry* 66, 239–244.
- Petegnief, V., Saura, J., Dewar, D., Cummins, D.J., Dragunow, M., Mahy, N., 1999. Long-term effects of alpha-amino-3-hydroxy-5-methyl-4-isoxazole propionate and 6-nitro-7-sulphamoylbenzo(f)quinoxaline-2,3-dione in the rat basal ganglia: calcification, changes in glutamate receptors and glial reactions. *Neuroscience* 94 (1), 105–115.
- Puchtler, H., Sweat, F., Levine, M., 1962. On the binding of Congo red by amyloid. *J. Histochem. Cytochem.* 10, 355–364.
- Quintana, C., Bellefqih, S., Laval, J.Y., Guerquin-Kern, J.L., Wu, T.D., Avila, J., Ferrer, I., Arranz, R., Patino, C., 2006. Study of the localization of iron, ferritin, and hemosiderin in Alzheimer's disease hippocampus by analytical microscopy at the subcellular level. *J. Struct. Biol.* 153 (1), 42–54.
- Reinus, W.R., Kyriakos, M., Gilula, L.A., Brower, A.C., Merkel, K., 1993. Plasma cell tumors with calcified amyloid deposition mistaken for chondrosarcoma. *Radiology* 189 (2), 505–509.
- Robinson, S.R., Bishop, G.M., 2002. Abeta as a bioflocculant: implications for the amyloid hypothesis of Alzheimer's disease. *Neurobiol. Aging* 23 (6), 1051–1072.

- Rodriguez, M.J., Bernal, F., Andres, N., Malpesa, Y., Mahy, N., 2000. Excitatory amino acids and neurodegeneration: a hypothetical role of calcium precipitation. *Int. J. Dev. Neurosci.* 18 (2–3), 299–307.
- Sadowski, M., Pankiewicz, J., Scholtzova, H., Li, Y.S., Quartermain, D., Duff, K., Wisniewski, T., 2004. Links between the pathology of Alzheimer's disease and vascular dementia. *Neurochem. Res.* 29 (6), 1257–1266.
- Sano, Y., Mihara, M., Miyamoto, T., Shimao, S., 1990. Simultaneous occurrence of calcification and amyloid deposit in pilomatricoma. *Acta Derm. Venereol.* 70 (3), 256–259.
- Schmued, L.C., Hopkins, K.J., Fluoro-Jade, B., 2000. A high affinity fluorescent marker for the localization of neuronal degeneration. *Brain Res.* 874 (2), 123–130.
- Slodzian, G., Daigne, B., Girard, F., Boust, F., Hillion, F., 1992. Scanning secondary ion analytical microscopy with parallel detection. *Biol. Cell* 74 (1), 43–50.
- Stewart, G.R., Olney, J.W., Schmidt, R.E., Wozniak, D.F., 1995. Mineralization of the globus pallidus following excitotoxic lesions of the basal forebrain. *Brain Res.* 695 (1), 81–87.
- Thompson, K.J., Shoham, S., Connor, J.R., 2001. Iron and neurodegenerative disorders. *Brain Res. Bull.* 55 (2), 155–164.
- Vanhoutte, G., Dewachter, I., Borghgraef, P., Van Leuven, F., Van der Linden, A., 2005. Noninvasive in vivo MRI detection of neuritic plaques associated with iron in APP[V717I] transgenic mice, a model for Alzheimer's disease. *Magn. Reson. Med.* 53 (3), 607–613.
- Watt, F., 1996. Nuclear microscope analysis in Alzheimer's and Parkinson's disease: a review. *Cell. Mol. Biol. (Noisy-le-grand)* 42 (1), 17–26.
- Wirhth, O., Multhaup, G., Czech, C., Blanchard, V., Moussaoui, S., Tremp, G., Pradier, L., Beyreuther, K., Bayer, T.A., 2001. Intraneuronal Abeta accumulation precedes plaque formation in beta-amyloid precursor protein and presenilin-1 double-transgenic mice. *Neurosci. Lett.* 306 (1–2), 116–120.